Non-identifiability of the Rayleigh damping material model in Magnetic Resonance Elastography

Andrii Y. Petrov*

Centre for Bioengineering, Department of Mechanical Engineering, University of Canterbury, Christchurch, New Zealand

Geoffrey J. Chase

Department of Mechanical Engineering, University of Canterbury, Christchurch, New Zealand

Mathieu Sellier

Department of Mechanical Engineering, University of Canterbury, Christchurch, New Zealand

Paul D. Docherty

Department of Mechanical Engineering, University of Canterbury, Christchurch, New Zealand

---

Abstract

Magnetic Resonance Elastography (MRE) is an emerging imaging modality for quantifying soft tissue elasticity deduced from displacement measurements within the tissue obtained by phase sensitive Magnetic Resonance Imaging (MRI) techniques. MRE has potential to detect a range of pathologies, diseases and cancer formations, especially tumors. The mechanical

*Corresponding author

Email addresses: andrew.petrov@pg.canterbury.ac.nz (Andrii Y. Petrov), geoff.chase@canterbury.ac.nz (Geoffrey J. Chase), mathieu.sellier@canterbury.ac.nz (Mathieu Sellier), paul.docherty@canterbury.ac.nz (Paul D. Docherty)

model commonly used in MRE is linear viscoelasticity (VE). An alternative Rayleigh damping (RD) model for soft tissue attenuation is used with a subspace-based nonlinear inversion (SNLI) algorithm to reconstruct viscoelastic properties, energy attenuation mechanisms and concomitant damping behavior of the tissue-simulating phantoms. This research performs a thorough evaluation of the RD model in MRE focusing on unique identification of RD parameters, μ_I and ρ_I.

Results show the non-identifiability of the RD model at a single input frequency based on a structural analysis with a series of supporting experimental phantom results. The estimated real shear modulus values (μ_R) were substantially correct in characterising various material types and correlated well with the expected stiffness contrast of the physical phantoms. However, estimated RD parameters displayed consistent poor reconstruction accuracy leading to unpredictable trends in parameter behaviour. To overcome this issue, two alternative approaches were developed: 1) simultaneous multi-frequency inversion; and 2) parametric-based reconstruction. Overall, the RD model estimates the real shear shear modulus (μ_R) well, but identifying damping parameters (μ_I and ρ_I) is not possible without an alternative approach.

Keywords:

Magnetic resonance elastography, nonlinear inversion, Rayleigh damping, model identifiability, mechanical properties, medical imaging

---

1. Introduction

Soft tissue property identification is valuable to a number of medical applications, such as diagnostic purposes [1–3], surgery simulations [4**?**], and virtual-reality based techniques. The elastic properties of soft tissues are closely related to their consistency, biological structure, and pathological conditions. Therefore, imaging of mechanical properties of tissue *in-vivo* can improve non-invasive tissue characterisation and help in early diagnosis of various pathologies.

Magnetic Resonance Elastography (MRE) can directly visualise and measure tissue elasticity [5–8], and has been applied to resolve stiffness characteristics of a variety human tissues and organs, such as muscle [9–12], breast [13–17], liver [18–20] and the brain [21–29]. MRE acquisition requires application of mechanical waves to tissue within the MRI, phase-contrast MR pulse sequence extended with motion encoding gradient (MEGs), and sophisticated inverse problem methods to identify an elastic modulus map of the tissue.

The choice of the constitutive model is crucial for accurate reproduction of the observed mechanical response. To date, reconstruction approaches generally assumed tissue to be linearly elastic [30], although some groups have employed more advanced models, such as viscoelasticity (VE) [23, 26, 27] and poroelasticity [31]. Rayleigh damping (RD) is an extension of VE, which utilises an additional damping parameter to provide a more complex description of the elastic energy attenuation.

Additional damping effects can improve model accuracy by providing a better data-model correlation [32]. In biological tissue, attenuation, or

damping, occurs due to the complex interaction between micro structural components in the soft tissue matrix. Therefore, the model that more accurately maps damping properties might bring additional diagnostic potential with regards to differentiating tissue structure and composition. Depending on consistency, this particular tissue type can display different damping properties. More specifically, tissue composed from tightly arranged cells displays less damping compared to the highly-saturated porous tissue. Thus, accurate quantification of damping properties might aid in early diagnosis of various degenerative diseases, such as Alzheimer's disease [23], Normal Pressure Hydrocephalus (NPH) [33] and Multiple Sclerosis (MS) [26].

The RD model incorporates attenuation behavior proportionally related to both elastic and inertial forces, which in the time-harmonic case can be implemented by the use of a complex shear modulus (μ_I) and a complex density (ρ_I) [34]. The use of a complex shear modulus also occurs when a viscoelastic material model is used and attributed here as an *elastic damping*. Damping resulting from the complex density can be associated with the damping force which is proportional to the velocity, and is referred here as an *inertial damping*. Therefore, the RD model allows extraction of two damping parameters, compared to standard VE models, commonly used in elastography, that use only complex shear modulus and a single damping parameter.

Identifying those two parameters and the resulting damping ratio (ξ_d), which is the ratio between these two damping parameters, could improve characterisation of the tissue composition and thus differentiation of various pathological processes in the tissue. However, the identifiably of the RD

model has yet to be demonstrated, and the subspace method, previously applied in phantoms and *in vivo* breast tissue for elastic material models [13, 35], has not been proven for the RD case.

The ability to uniquely recover unknown parameters is a fundamental prerequisite in the model development. Although a variety of methods have been proposed to test identifiability of nonlinear models [36–38], it remains a challenging mathematical problem. In this paper we present a full structural analysis of the linear RD elastic model, which is supported by MRE phantom experiments. In this regard, the limitations associated with the use of a RD model applied to time-harmonic MRE are presented and discussed both analytically and experimentally.

2. Materials and methods

2.1. Subspace-based image reconstruction algorithm

Elastographic image reconstruction is performed using a proven subspace-based nonlinear inversion (SNLI) algorithm [39] that is formulated as an iterative constrained optimisation that minimises the objective function:

$$\Phi(\boldsymbol{\theta}) = \sum_{i=1}^{N_m} (\mathbf{u}_i^m - \mathbf{u}_i^c(\boldsymbol{\theta}))(\mathbf{u}_i^m - \mathbf{u}_i^c(\boldsymbol{\theta}))^H, \tag{1}$$

where $\mathbf{u}_i^m$ represents the complex valued measured displacement data at i'th measurement point, $\mathbf{u}_i^c(\boldsymbol{\theta})$ is the co-located displacement calculated by a forward simulation of the model using a current estimate of the properties ($\boldsymbol{\theta}$), N_m is the number of measurements and the superscript ^{H} denotes the complex conjugate transpose. In MRE, the number of measurements corresponds to the number of measured displacements. The minimisation is performed

by updating $\boldsymbol{\theta}$ using the conjugate-gradient (CG) method [40]. Calculation of $\mathbf{u}_i^c(\boldsymbol{\theta})$ is referred as the *forward computational problem*, and the process of iterative estimation of the material property parameters $\boldsymbol{\theta}$ that minimize Eq. 1 is the *inverse problem*. Regularisation techniques, such as spatial filtering (SF), total variation (TV) minimisation [41] and parameter constrains are applied to further stabilise the inversion process.

The forward problem for SNLI requires the solution of system of linear partial differential equations (PDEs). For this study, a finite element (FE) implementation of an isotropic linear nearly-incompressible RD material model was used, to account for a nearly-incompressible behavior expected in the tofu material due to the high water content. The motion amplitude, $\mathbf{u}$, is calculated from Navier's equation:

$$\nabla \cdot (\mu(\nabla \mathbf{u} + \nabla \mathbf{u}^T)) - \nabla(\frac{1}{3}\nabla \cdot \mathbf{u}) - \nabla P = -\rho\omega^2 \mathbf{u}; \tag{2}$$

where $\mathbf{u}$ is the displacement within the medium; λ is the first Lamé's parameter, μ is the second Lamé's parameter, also known as a shear stiffness; ρ is the density of the material, ∇P is a pressure term, related to volumetric changes through the bulk modulus, K.

2.2. RD model

Navier's equation with damping can be discretised:

$$\mathbf{M}\ddot{\mathbf{u}} + \mathbf{C}\dot{\mathbf{u}} + \mathbf{K}\mathbf{u} = \mathbf{f} \tag{3}$$

where $\mathbf{M}$, $\mathbf{C}$ and $\mathbf{K}$ are mass, damping and stiffness matrices, $\mathbf{u}$ is the displacement vector ($\dot{\mathbf{u}}$ and $\ddot{\mathbf{u}}$ correspond to the first and second time deriva-

tives), and $\mathbf{f}$ represents external and body forces. In time-harmonic steady state elastography, motion and forces can be defined as $\mathbf{u}(\mathbf{x},t) = \hat{\mathbf{u}}(\mathbf{x})e^{i\omega t}$ and $\mathbf{f}(\mathbf{x},t) = \hat{\mathbf{f}}(\mathbf{x})e^{i\omega t}$, yielding:

$$(-\omega^2\mathbf{M} + i\omega\mathbf{C} + \mathbf{K})\hat{\mathbf{u}} = \hat{\mathbf{f}} \tag{4}$$

In a RD system, the damping is directly proportional to the mass and stiffness, $\mathbf{C} = \alpha\mathbf{M} + \beta\mathbf{K}$:

$$\left[-\omega^2\left(1 - \frac{i\alpha}{\omega}\right)\mathbf{M} + (1 + i\omega\beta)\,\mathbf{K}\right]\hat{\mathbf{u}} = \hat{\mathbf{f}} \tag{5}$$

where $\mathbf{K}$ and $\mathbf{M}$ are initial undamped stiffness and mass distributions, respectively. All coefficients in $\mathbf{M}$ contain the density, ρ, and all coefficients in $\mathbf{K}$ contain the shear modulus, μ. Thus, these parameters can be moved outside the matrices, giving:

$$\left[-\omega^2\left(\rho - \frac{i\alpha\rho}{\omega}\right)\mathbf{M}' + (\mu + i\omega\beta\mu)\,\mathbf{K}'\right]\hat{\mathbf{u}} = \hat{\mathbf{f}}, \tag{6}$$

where $\mathbf{M}' = (1/\rho)\mathbf{M}$ and $\mathbf{K}' = (1/\mu)\mathbf{K}$ are the normalised mass and stiffness matrices, respectively. Eq. 6 indicates that the RD model can be implemented using a complex density $\rho^* = \rho_R + i\rho_I$ and complex shear modulus $\mu^* = \mu_R + i\mu_I$. The physical interpretation of the μ_R and μ_I is the storage and loss modulus of the material, while ρ_I for a nearly-incompressible material is hypothesised to indicate fluid perfusion within the solid elastic matrix of the porous media. In other words, μ_R and ρ_R describe the real stiffness and density in the undamped system, while μ_I and ρ_I represent damping due to the elastic and inertial forces, respectively; and can be expressed in terms of the RD parameters [34]:

$$\rho_I = \frac{-\alpha\rho_R}{\omega}, \qquad \mu_I = \omega\beta\mu_R \tag{7}$$

Considering that the terms $(1 - i\alpha/\omega)$ and $(1 + i\omega\beta)$ carry the spatial information of RD parameters, Eq. 6 can be further simplified:

$$\Big[-\omega^2\rho^*\mathbf{M}' + \mu^*\mathbf{K}' \Big]\hat{\mathbf{u}} = \hat{\mathbf{f}} \tag{8}$$

The resulting damping ratio, ξ_d, is defined:

$$\xi_d = \frac{1}{2}\left(\frac{\alpha}{\omega} + \beta\omega\right) \quad \Rightarrow \quad \xi_d = \frac{1}{2}\left(\frac{\mu_I}{\mu_R} - \frac{\rho_I}{\rho_R}\right) \tag{9}$$

The RD model allows reconstruction of not only the stiffness distribution (μ_R), but also energy attenuation mechanisms proportionally related to both elastic (μ_I) and inertial (ρ_I) effects. This approach may allow better description of the microscale interactions that cause motion attenuation, compared to the more commonly used viscoelastic model, which does not incorporate inertial damping effects.

Accurate reconstruction of the RD parameters may bring additional diagnostic potential with regards to differentiation of various tissue types and more accurate characterisation of certain pathological diseases based on different energy absorbing mechanisms. Therefore, the RD model offers reconstruction of three material properties (μ_R, μ_I, ρ_I) that can contain clinical diagnostic merit in contrast to only two (μ_R, μ_I) for the VE case.

2.3. Inertial explanation of the RD model

In the RD model, Newton's 2^{nd} law of motion defines the body force ($\mathbf{b}$) due to inertial forces as:

$$\mathbf{b} = \frac{\partial\left(\rho\dot{\mathbf{u}}\right)}{\partial t} = \frac{\partial\rho}{\partial t}\frac{\partial\mathbf{u}}{\partial t} + \rho\frac{\partial^2\mathbf{u}}{\partial t^2} \tag{10}$$

where $\rho\dot{\mathbf{u}}$ is the momentum of the system. For a time-harmonic system, where the time-dependent behavior of a complex-valued $\mathbf{u} = \mathbf{u}_R + i\mathbf{u}_I$ at angular frequency ω is given by $\mathbf{u}(\mathbf{x}, t) = \Re\Big\{\hat{\mathbf{u}}e^{i\omega t}\Big\}$, one obtains:

$$\begin{aligned}
\frac{\partial\mathbf{u}}{\partial t} &= \Re\Big\{i\omega\hat{\mathbf{u}}e^{i\omega t}\Big\} = -\omega\Big[\mathbf{u}_R\sin\omega t + \mathbf{u}_I\cos\omega t\Big], \\
\frac{\partial^2\mathbf{u}}{\partial t^2} &= \Re\Big\{-\omega^2\hat{\mathbf{u}}e^{i\omega t}\Big\} = -\omega^2\Big[\mathbf{u}_R\cos\omega t - \mathbf{u}_I\sin\omega t\Big].
\end{aligned} \tag{11}$$

Substituting Eq. 11 into Eq. 10, leads to the inertial force description:

$$\mathbf{b} = -\omega\frac{\partial\rho}{\partial t}(\mathbf{u}_R\sin\omega t + \mathbf{u}_I\cos\omega t) - \omega^2\rho(\mathbf{u}_R\cos\omega t - \mathbf{u}_I\sin\omega t), \tag{12}$$

where the term $\partial\rho/\partial t$ describes changes in density occurring at angular frequency ω and justifies the inclusion of the an inertial term in the model.

Time-harmonic formulation of a RD elastic system results in a complex density, $\rho^* = \rho_R + i\rho_I$, which scales the acceleration term in the elastic equilibrium equation to give the inertial body forces for the system defined:

$$\mathbf{b} = \rho\frac{\partial^2\mathbf{u}}{\partial t^2} = -\omega^2\Big[\left(\rho_R\mathbf{u}_R - \rho_I\mathbf{u}_I\right)\cos\omega t - \left(\rho_I\mathbf{u}_R + \rho_R\mathbf{u}_I\right)\sin\omega t\Big]. \tag{13}$$

Comparing the inertial body forces given by Eqs. 12 & 13, yields:

$$\begin{aligned}
&-\omega\frac{\partial\rho}{\partial t}(\mathbf{u}_R\sin\omega t + \mathbf{u}_I\cos\omega t) - \omega^2\rho(\mathbf{u}_R\cos\omega t - \mathbf{u}_I\sin\omega t)\cdots \\
&\cdots = -\omega^2\Big[\left(\rho_R\mathbf{u}_R - \rho_I\mathbf{u}_I\right)\cos\omega t - \left(\rho_I\mathbf{u}_R + \rho_R\mathbf{u}_I\right)\sin\omega t\Big]
\end{aligned} \tag{14}$$

Simplifying and collecting terms leads to equivalences defined:

$$\frac{\partial \rho}{\partial t} = -\omega \rho_I \quad \Rightarrow \quad \rho_I = -\frac{1}{\omega}\frac{\partial \rho}{\partial t} \tag{15}$$

$$\omega \rho = \omega \rho_R \quad \Rightarrow \quad \rho_R = \rho. \tag{16}$$

Eq. 15 indicates that ρ_I describes the time change in density scaled by the angular frequency, ω. For a compressible material, this change in density would indicate some level of compression within the material. However, for a nearly-incompressible or saturated porous material, this change would represent the fluid perfusion within the solid elastic matrix. To ensure that the energy is lost from the system due to this mass transfer, rather than gained, it is important to ensure that $\rho_I < 0$.

Eq. 16 shows that ρ_R describes the actual density of the continuum, as expected. Therefore, in a porous media, rheological interpretation of the imaginary density term would be associated with the rate of density change in the porous voxel due to the volume fraction between fluid and solid compartments. Overall, it is clear that the RD model with ρ_I, μ_I offers better option to define all modes of energy dissipation in biological tissue compared to a simpler VE model.

2.4. Structural analysis of the RD model

Structural model analysis was performed to investigate the identifiably of the RD model parameters. The analysis assessed parameter uniqueness using a typical input-output approach. The input-output method summarises the complete relationship between the input-output structure of the model and determines the identifiably of each estimated parameter [38, 42].

2.5. Experimental methodology

2.5.1. Phantom experiments

Two phantoms were generated using partial geometries of tofu and gelatine. Tofu is known to possess a porous microstructure, which is composed of an organic solid matrix with pores of different sizes and shapes. Therefore, it has been proposed recently as a sonographic and elastographic tissue-mimicking material with acoustic and mechanical properties similar to those of some soft tissues [43, 44].

The first phantom (P1) was made of soft tofu slab of $105 \times 80 \times 45$ mm, with a single, stiff gelatine inclusion (10% concentration, Sigma Aldrich). The second phantom (P2) was a reverse configuration of P1, with stiff 10% concentration of a gelatine as the background and a soft tofu as the inclusion. Both phantoms had an external rectangular shape with a cylindrical inclusion located at the centre. Piezo-electric actuation was utilized to introduce shear waves into the phantoms at mechanical frequencies of 50 Hz, 75 Hz, 100 Hz and 125 Hz. The phantoms were positioned on the actuation plate attached to the piezoelectric driver. The actuation direction induced by piezoelectric driver was in the Y direction causing propagation of the shear strain waves in the phantom in the Z direction (refer to Fig 1).

MRE imaging experiments were performed on a 1.5 T Philips MRI scanner. 20 coronal slices of 2 mm thickness of 3D steady-state displacement fields were acquired by an spin-echo based phase-contrast sequence, extended with trigger timing and MEG modules, using the following parameters: TR/TE = 480/10 ms; FOV = $150 \times 225 \times 40$ mm and 2 mm^3 isotropic voxel. A 3D quality-guided phase unwrapping method [45] was applied to the motion

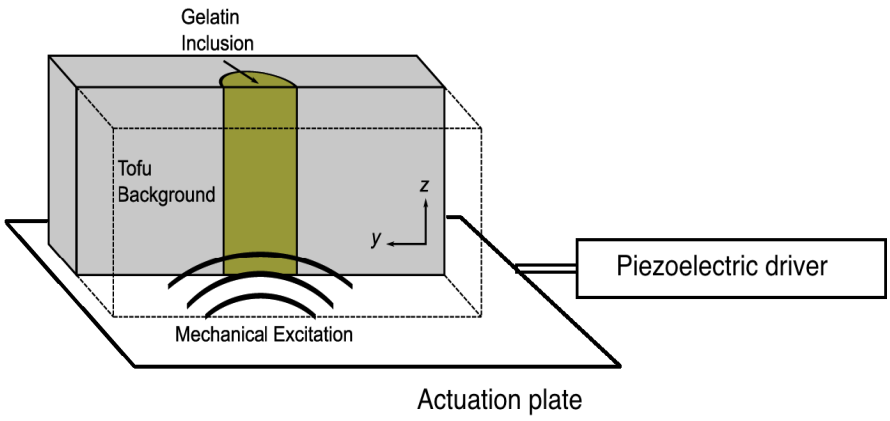

Figure 1: An illustrative drawing of the cross-section of a tofu phantom ($100 \times 75 \times 45$ mm) containing a 28.5 mm diameter cylindrical inclusion that passes vertically through centre of the slab.

MRE data to suppress phase wrapping. The reconstruction results were then analysed to evaluate the presence of statistically significant differences among the two types of materials and for image quality analysis. The background and inclusions were segmented to calculate the median and the interquartile range (IQR) of the material property values.

2.5.2. Reconstruction protocol

A SNLI algorithm [39, 46] was used to estimate material properties from measured MR displacement data. Reconstruction computations were carried out on High Performance Computing (HPC) system *Blue Fern P575*. A total of 32 processors were employed in parallel message passing interface (MPI) environment to produce 100 global iterations using CG optimisation method. The average runtime for the reconstruction processing was 5 hours.

Each parameter was interpolated at different resolution levels [47].

Reconstruction of material properties using an isotropic linearly elastic nearly-incompressible RD material model was performed using the following parameters: an isotropic subzone size of $24 \times 24 \times 24$ mm with the subzone overlap of $0.15 \times 0.15 \times 0.15$ %. Displacements were approximated on the FE mesh with $1.8 \times 1.8 \times 1.9$ mm voxel resolution, providing approximately 16 nodes per wavelength for the FE forward problem. Initial *a-priori* estimates were $\mu_R = 3300$ Pa, $\mu_I = 330$ Pa and $\rho_I =$ -100 kg/m^3. The real density (ρ_R) and the bulk modulus (K) were set to constants, where $\rho_R = 1000$ kg/m^3 and $K = 10^7$ Pa to account for nearly-incompressible behaviour expected in a highly saturated media, such as the tofu material.

To minimise the risk of obtaining unrealistic solutions of the material property values, the parameter inbox constraints were imposed along with other applied regularisation techniques, such as the Tikhonov regularisation [48], the total variation minimisation (TVM) [41], and spatial filtering (SF). The minimum and maximum values for inbox constraints were: μ_R (200 Pa - 50 kPa), μ_I (1 Pa - 10 kPa), and ρ_I (- 5000 kg/m^3 - -1 kg/m^3). The initial and final TV weighting was 10^{-15} and 10^{-14} with TV delta set to 10^{-19}. The initial and final SF weights were set to 0.25 % and 0.15 % respectively.

Convergence was declared after approximately 100 iterations. More specifically, after 100 iterations the change in the median parameter values was $<$ 0.1% of the final parameter value. Convergence criteria was achieved for all material properties in phantom reconstructions. Stabilisation of statistical indicators, such as the median and associated percentiles of parameter behaviour for all nodes within FE mesh across computed iterations was used

to evaluate of the convergence for a particular parameter.

3. Results

3.1. Structural analysis of the RD model

Based on Eq. 7, the RD coefficients, α and β, can be formulated as:

$$\alpha = \frac{-\omega\rho_I}{\rho_R}, \qquad \beta = \frac{\mu_I}{\omega\mu_R}. \tag{17}$$

Considering that all terms in $\mathbf{M}$ contain the density (ρ_R) and all terms in $\mathbf{K}$ contain the shear modulus (μ_R), then for a single degree of freedom system by substituting Eq. 17 into Eq. 6 results:

$$\left[-\omega^2\rho_R + i\omega\left(\frac{-\omega\rho_I}{\rho_R}\rho_R + \frac{\mu_I}{\omega\mu_R}\mu_R\right) + \mu_R\right]\hat{\mathbf{u}} = \hat{\mathbf{f}}, \tag{18}$$

$$\left[-\omega^2\rho_R + i\omega\left(\frac{\mu_I}{\omega} - \omega\rho_I\right) + \mu_R\right]\hat{\mathbf{u}} = \hat{\mathbf{f}} \tag{19}$$

Collecting the coefficients of the $\Re$ and $\Im$ terms yields:

$$\Big[-\omega^2\rho_R + \mu_R\Big]\mathbf{u}_R + \Big[\mu_I - \omega^2\rho_I\Big]\mathbf{u}_I = \hat{\mathbf{f}}. \tag{20}$$

Eq. 20 indicates that the real displacement, $\mathbf{u}_R$, is described by two parameters μ_R and ρ_R. In RD reconstruction, the real density (ρ_R) is assumed to be a density of a water, e.g. $\rho_R = 1000$ kg/m^3. Therefore, $\mathbf{u}_R$ is defined by two model parameters and only one variable μ_R. Hence, μ_R is easily and uniquely identifiable being a direct function of the real displacements: $\mu_R = f(\mathbf{u}_R)$.

However, $\mathbf{u}_I$ is determined by two model parameters, ρ_I and μ_I, which are both variables. Hence, both parameters can have a model role, but

there cannot be unique identification of those variables at one frequency without further *a-priori* information. Therefore, the overall RD model is not identifiable. However, results exist for reconstruction. The following experimental results are used to clearly illustrate this outcome.

3.2. Phantom experiments

Fig. 2 shows the T2*- weighted MR images for P1 and P2 phantoms. Fig. 3 shows the full simultaneous three parameter-based RD reconstruction results of P1 and P2 phantoms at 75 Hz. The results show significant failure to differentiate materials clearly in the reconstructed μ_I and ρ_I images. Damping has also not been clearly differentiated. Fig. 4 supports Fig. 3 by showing a lot of overlap and lack of separation between materials for μ_I and ρ_I for both phantoms, whereas μ_R is more clear. In addition, Tables 1 and 2 present summary of quantified results for both phantoms across multiple frequencies.

Fig. 5 illustrates three parameter-based RD and two parameter VE reconstruction results of the P1 phantom at 125 Hz. Similar qualitative as well as quantitative results are observed for μ_R, μ_I and ξ_d reconstructions, indicating non-identifiable nature of the ρ_I parameter. Finally, Fig. 6 shows octahedral shear strain SNR (OSS-SNR) distribution results for both phantom configurations at 75 Hz. Generally, high SNR level (above 5) is seen in both phantoms, which would normally indicate a good reconstruction.

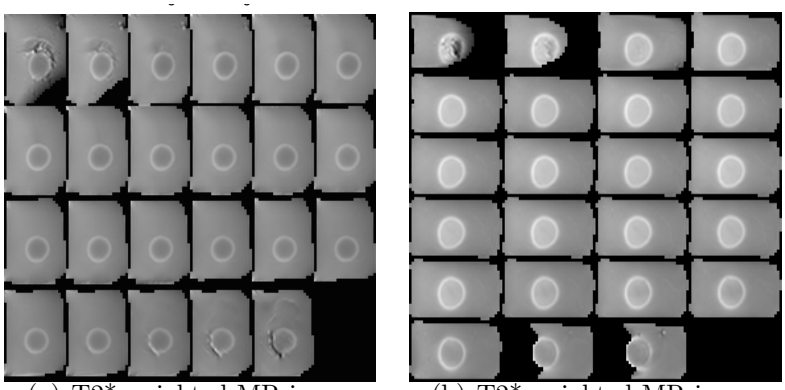

(a) T2*-weighted MR image (b) T2*-weighted MR image

Figure 2: MRI image results of the P1 and P2 phantoms (a) P1 phantom and (b) P2 phantom.

Table 1: Quantitative ROI analysis of the P1 phantom for multiple frequencies

Parameter Units	MA (μm) Median [IQR]	μ_R (Pa) Median [IQR]	μ_I (Pa) Median [IQR]	ρ_I (kg/m^3) Median [IQR]	ξ_d (% / 100) Median [IQR]
Gelatine (50 Hz)	1.42 [1.37 – 1.56]	4926 [4763 – 5052]	3.6 [2.8 – 6.6]	-4 [-13 – -2]	0.0038 [0.0013 – 0.0125]
Gelatine (75 Hz)	1.64 [1.56 – 1.80]	8372 [8053 – 8635]	80 [63 – 98]	-13[-20 – -5]	0.014 [0.001 – 0.020]
Gelatine (100 Hz)	2.33 [2.29 – 2.39]	11638 [10680 – 12355]	31 [18 – 50]	-19 [-58 – -5]	0.012 [0.0037 – 0.0395]
Gelatine (125 Hz)	2.32 [2.10 – 2.49]	14790 [13838 – 15860]	51 [19 – 194]	-73[-108 – -39]	0.037 [0.020 0.054]
Soft tofu (50 Hz)	2 [1.56 – 2.54]	3288 [3034 – 3601]	85 [33 – 353]	-46 [-114 – -9]	0.066 [0.030 – 0.124]
Soft tofu (75 Hz)	1.92 [1.52 2.46]	3341 [3105 – 3624]	256 [123 – 393]	-85 [-192 – -32]	0.10 [0.07 – 0.14]
Soft tofu (100 Hz)	1.94 [1.65 – 2.33]	3590 [3327 – 4113]	109 [59 – 211]	-157 [-260 – -92]	0.11 [0.072 – 0.156]
Soft tofu (125 Hz)	1.79 [1.42 – 2.31]	4902 [4181 – 6128]	102 [30 – 325]	-401 [-658 – -130]	0.22 [0.11 – 0.34]

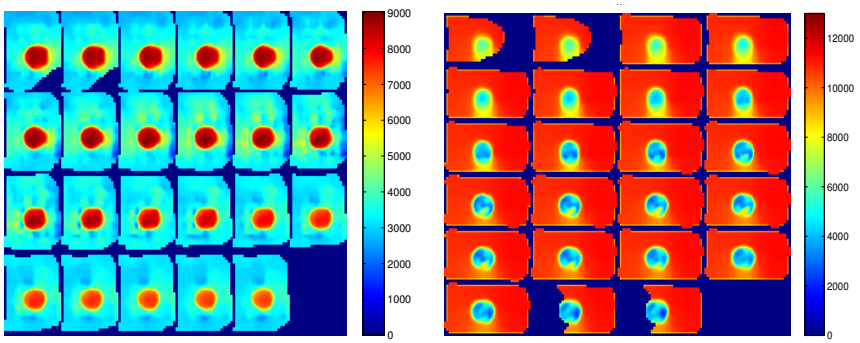

(a) μ_R (P1) (b) μ_R (P2)

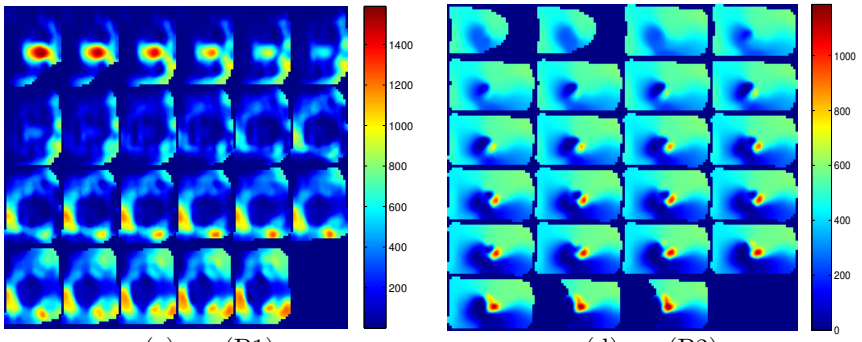

(c) μ_I (P1) (d) μ_I (P2)

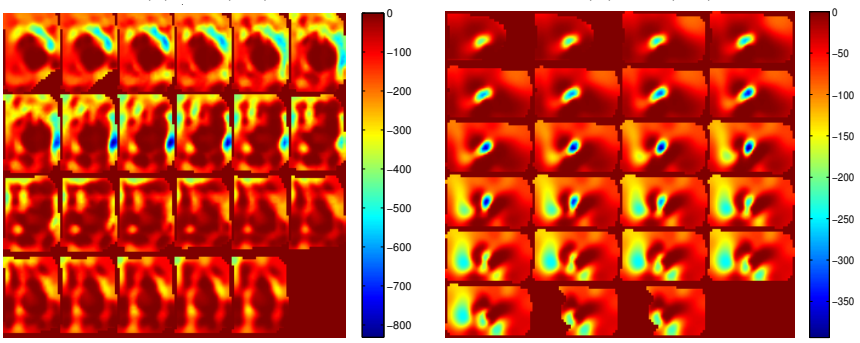

(e) ρ_I (P1) (f) ρ_I (P2)

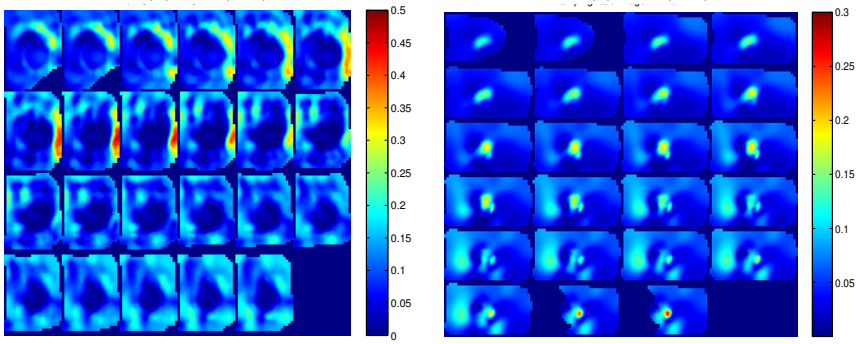

(g) ξ_d (P1) (h) ξ_d (P2)

Figure 3: Image results for the full simultaneous three parameter-based RD reconstruction of the P1 (soft tofu background with a single stiff gelatine inclusion) and P2 phantom (stiff gelatine background with a single soft tofu inclusion) using 75 Hz mechanical excitation: (a) and (b) storage modulus μ_R image (Pa); (c) and (d) loss modulus μ_I image (Pa); (e) and (f) imaginary density ρ_I image (kg/m^3), and (g) and (h) damping ratio ξ_d image (% / 100)

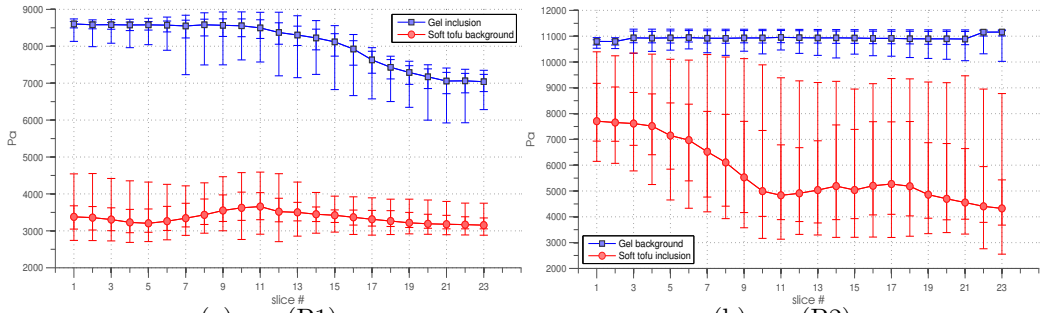

(a) μ_R (P1)

(b) μ_R (P2)

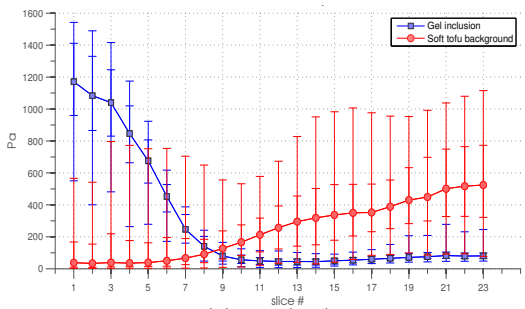

(c) μ_I (P1)

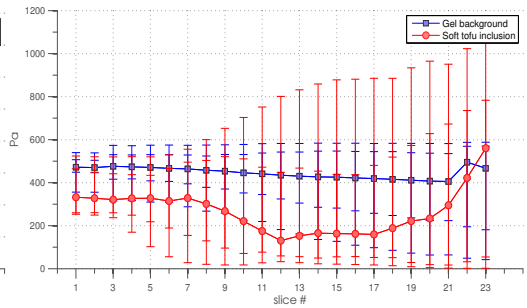

(d) μ_I (P2)

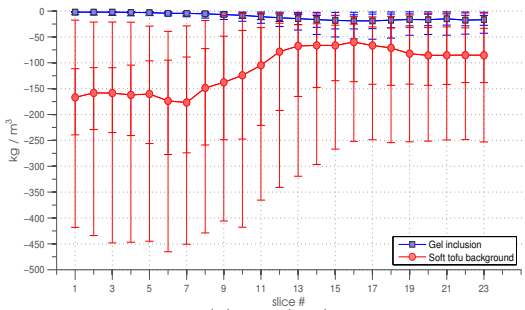

(e) ρ_I (P1)

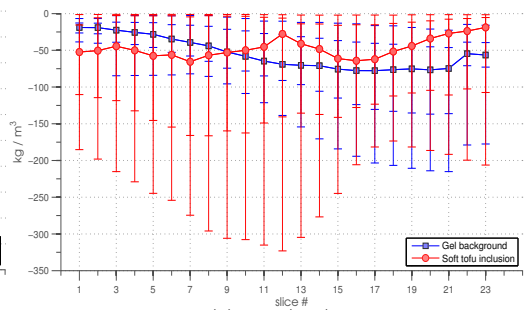

(f) ρ_I (P2)

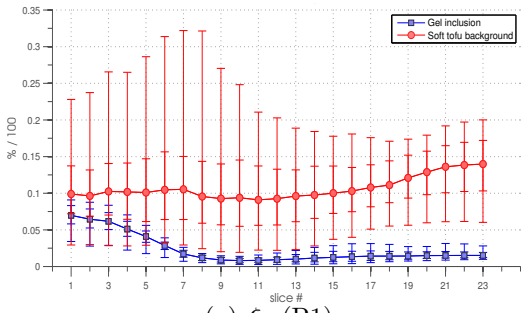

(g) ξ_d (P1)

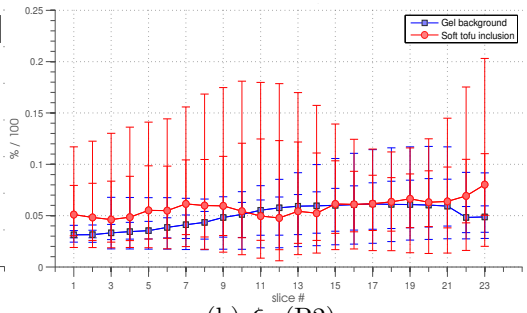

(h) ξ_d (P2)

Figure 4: Quantitative analysis of P1 and P2 phantoms at 75 Hz of both materials within the selected regions of interest (ROIs) for each material property: (a) and (b) storage modulus μ_R image (Pa); (c) and (d) loss modulus μ_I image (Pa); (e) and (f) imaginary density ρ_I image (kg/m^3), and (g) and (h) damping ratio ξ_d image (% / 100). Uncertainty bars represent the (5 25 50 75 95) percentiles.

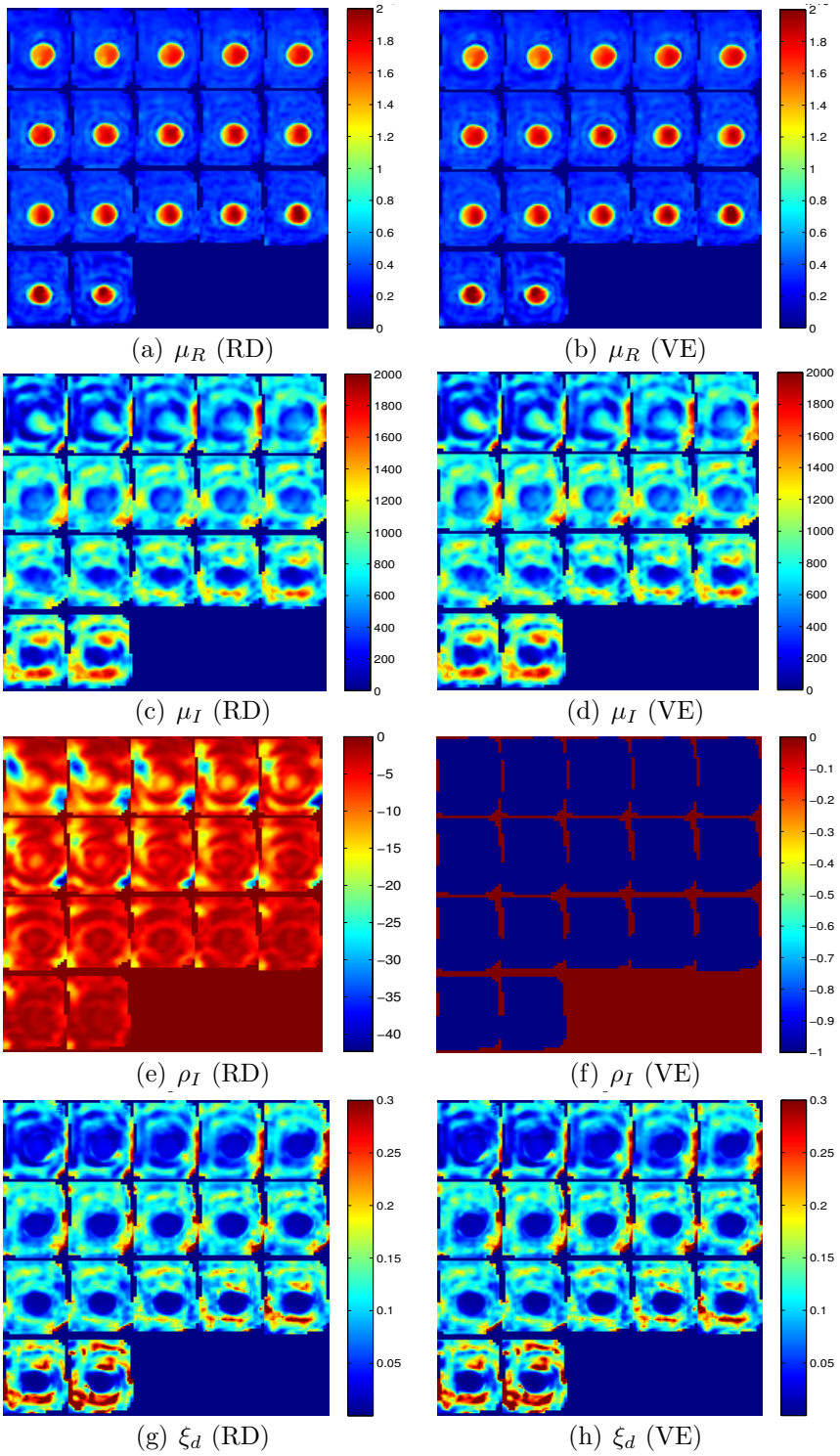

(a) μ_R (RD) (b) μ_R (VE)

(c) μ_I (RD) (d) μ_I (VE)

(e) ρ_I (RD) (f) ρ_I (VE)

(g) ξ_d (RD) (h) ξ_d (VE)

Figure 5: Image results for RD (left column) and VE (right column) reconstruction of the P1 phantom configuration at 125 Hz using same experimental protocol: (a) and (b) storage modulus μ_R image ($\times 10^4$ Pa); (c) and (d) loss modulus μ_I image (Pa); (e) and (f) imaginary density ρ_I image (kg/m^3), and (g) and (h) damping ratio ξ_d image (% / 100)

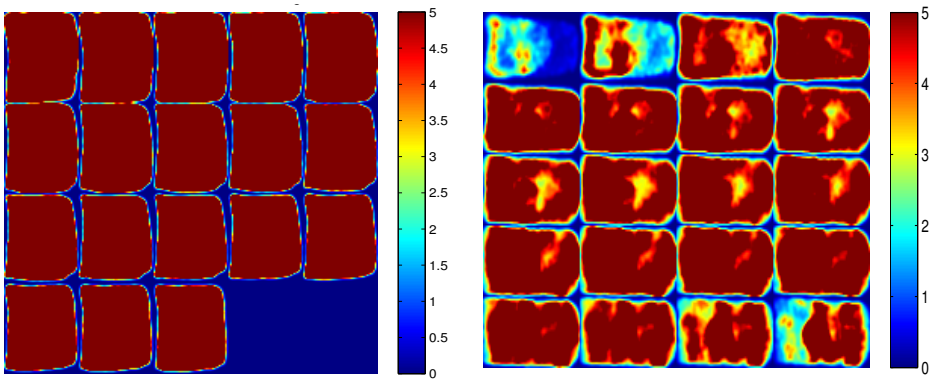

(a) OSS-SNR (P1) (b) OSS-SNR (P2)

Figure 6: Image results of the OSS-SNR distribution of the P1 and P2 phantoms at 75 Hz: a) P1 phantom and b) P2 phantom.

Table 2: Quantitative ROI analysis of the P2 phantom for multiple frequencies

Parameter Units	MA (μm)	μ_R (Pa)	μ_I (Pa)	ρ_I (kg/m^3)	ξ_d (% /100)
	Median [IQR]	Median [IQR]	Median [IQR]	Median [IQR]	Median [IQR]
Gelatine (50 Hz)	1.6 [1.34 – 1.86]	8920 [8435 – 9278]	276 [241 – 312]	-15 [-27 – -8]	0.024 [0.0193 – 0.032]
Gelatine (75 Hz)	1.75 [1.45 – 2]	10930 [10733 – 11202]	445 [324 – 537]	-58 [-78 – -28]	0.05 [0.03 – 0.062]
Gelatine (100 Hz)	1.77 [1.31 – 1.98]	14506 [14287 – 15911]	510 [394 – 551]	-47 [-81 – -23]	0.04 [0.028 – 0.054]
Gelatine (125 Hz)	1.72 [1.47 – 2.14]	16048 [15763 – 16714]	732 [474 – 866]	-63 [-117 – -25]	0.054 [0.036 – 0.082]
Soft tofu (50 Hz)	2.6 [2 – 3]	6688 [5661 – 7508]	161 [110 – 186]	-154 [-257 – -70]	0.088 [0.045 – 0.14]
Soft tofu (75 Hz)	2 [1.66 – 2.6]	5189 [4034 – 7679]	267 [59 – 472]	-50 [-132 – -6]	0.06 [0.03 – 0.098]
Soft tofu (100 Hz)	2.23 [1.8 – 2.64]	7200 [5378 – 9151]	137 [80 – 230]	-228 [-356 – -140]	0.12 [0.091 0.186]
Soft tofu (125 Hz)	1.85 [1.57 – 2.18]	8995 [6325 – 11550]	97 [42 – 210]	-262 [-500 – -83]	0.13 [0.05 – 0.25]

4. Discussion

4.1. Structural analysis

The structural analysis revealed non-identifiability of the RD model at a single frequency. Use of a non-uniquely identifiable model in a clinical setting will result in parameter values that do not capture the true material property even though the modelled displacement-data match. The resulting error in parameter estimation could lead to faulty diagnosis and unjustified conclusions. To overcome this issue two approached are postulated: 1) simultaneous multifrequency inversion, and 2) parametric-based inversion.

1. Simultaneous multifrequency inversion performs simultaneous identification on motion data from two or more input frequencies. Here, both parameters are frequency dependant. The current system is effectively a system of one equation with two unknowns, which is impossible to resolve without specifying either ρ_I or μ_I:

$$\begin{pmatrix} -\omega^2\mathbf{u}_I(t_1) & \mathbf{u}_I(t_1) \\ -\omega^2\mathbf{u}_I(t_2) & \mathbf{u}_I(t_2) \\ \vdots & \vdots \\ -\omega^2\mathbf{u}_I(t_n) & \mathbf{u}_I(t_n) \end{pmatrix} \begin{pmatrix} \rho_I \\ \mu_I \end{pmatrix} = \begin{pmatrix} \Im[\hat{\mathbf{f}}_1(t_1)] \\ \Im[\hat{\mathbf{f}}_1(t_2)] \\ \vdots \\ \Im[\hat{\mathbf{f}}_1(t_n)] \end{pmatrix} \begin{matrix} [1] \\ [2] \\ \\ [n] \end{matrix} \tag{21}$$

However, if two frequencies are used, one obtains two equations with two unknowns presuming ρ_I and μ_I can be related between the two frequencies by a power law or other relation.

Therefore, at least two frequencies are required for unique identification of the RD parameters. However, practical identifiability is not assured if both frequencies are within similar range. Thus, a wide range of input frequencies,

where $\omega_1 \gg \omega_2$ or $\omega_1 \ll \omega_2$ is essential for strong practical and theoretical identifiability [49].

2. Parametric-based inversion, where either ρ_I or μ_I is set to a constant or dependant function, thus, specifying its value. This approach yields a system effectively composing one equation with one unknown in Eq. 20 which is uniquely identifiable. It is important to stress that specifying μ_R does not solve the identifiability problem, as the imaginary components of the complex valued parameters are independent from their real components.

The parametric approach allows only a single value of a particular parameter to be globally declared throughout the reconstruction domain, thus automatically leading to a limitation of the RD model to accurately reconstruct two independent material regions characterised by different mechanical properties. A more robust approach of the parametrisation method would include specification of the multiple regions of interest (ROIs) corresponding to different materials, where specific mechanical properties can be defined for each individual region.

Overall, this study leads to a robust conclusion that RD model, applied to a time-harmonic MRE, is non-identifiable with regards to unique delineation of the RD parameters, ρ_I and μ_I, at a single frequency. In contrast, μ_R was captured relatively well, also confirming the outcome of that part of the identifiability analysis. Unique identification of the RD parameters at a single frequency is not possible due to the fundamental formulation of the RD model, which describes rate of damping change across multiple frequency modes. Therefore, at least two frequencies are required for reasonable fit of damping property data or a parametric approach is required.

4.2. Phantom experiments

Non-identifiability of the RD parameters at a single frequency is further confirmed by the MRE phantom experiments. The differences between the quality of reconstruction for the different parameters was evident, with the real shear modulus, μ_R, having the highest quality image and the images of the RD parameters, μ_I and ρ_I, being significantly poorer. These trends verify results from the structural model analysis.

Qualitatively, the μ_R reconstruction of both materials in the P1 phantom at 75 Hz was successful in confirming the higher stiffness of the gelatine inclusion compared to the soft tofu background. Opposite results were obtained for P2, as expected. Boundaries between the two materials were accurately delineated with no significant artefacts present. Generally, the μ_R behaviour within both materials is consistent throughout the phantom as confirmed by plotted median values in Figs. 4 (a) and 4 (b). The variation in the distribution of the μ_R values within both materials was found to be relatively low, as confirmed by the IQR values given in Tables 1 and 2.

The reconstructed RD parameters from both phantoms yielded impractical material property estimates. In particular, Tables 1 and 2 show that the parameter values did not accurately or precisely assess expected outcomes for ρ_I and μ_I. More specifically, reconstruction quality of the μ_I and ρ_I was relatively poor around material boundaries and within the homogeneous material regions (refer to Figs. 3 (c)-(f)). Unexpected trends in parameter behaviours associated with weak characterisation of the both damping properties material types was generally observed, as seen in Figs. 4 (c)-(f).

Qualitatively, ξ_d reconstruction in P1 at 75 Hz (refer to Fig. 3 (g)) had a

moderate success. In P2, ξ_d images generally identified presence of the tofu inclusion, correctly confirming higher loss of mechanical energy in the more attenuating tofu material compared to the stiffer gelatine background across multiple frequencies. However, accurate characterisation of both materials as well as delineation of the boundaries failed, as shown in Fig. 3 (h).

Fig. 5 shows the RD and VE reconstruction results of the P1 phantom at 125 Hz. Despite using two different models, no change in μ_I and ξ_d parameters was observed. These results confirm inaccurate identification of the ρ_I parameter in RD reconstruction, which is introduced to compensate for the lack of identifiability using one parameter to ensure minimal parameter identification. Hence, in the RD model, both μ_I and ρ_I parameters do not reflect realistic behaviour and therefore are misleading due to this lack of identifiability despite high SNR and convergence.

The obtained results indicate that accurate delineation of the RD based properties and concomitant damping ratio at a single frequency is very difficult even with the number of regularisation techniques applied to the SNLI. Given that in RD formulation the shear modulus and density are complex-valued quantities, elastographic reconstruction of the RD properties, represented as the unknown imaginary components, is not possible at a single frequency due to the non-identifiable formulation of the model composition. Therefore, reconstructed complex RD properties will not have meaning, which casts doubt on same uses of this model in inverse problem.

The phantom experiments allow better understanding the limitations of the RD reconstructions to distinguish damping in these types of materials. Preliminary RD MRE experiments on a similar to the P1 phantom configu-

ration were performed by Van Houten *et al* [50] where reconstruction results produced by the RD model were compared to the reconstruction results computed by linear VE model. The parameters investigated were effectively the real shear modulus (μ_R) and a damping ratio (ξ_d). However, this study emphasises the need for further assessment of the RD model to accurately delineate the RD parameters, μ_I and ρ_I, where the lack of identifiability is clearly evident.

4.3. OSS-SNR

Producing accurate, reliable estimates of the mechanical properties of tissue with SNLI algorithm is critically dependent on the quality of the acquired MRE displacement images. In this research, data quality is estimated using OSS-SNR measure [51]. The strain SNR signal is directly proportional to the wavelength of a propagating shear strain wave which is determined by the excitation frequency and stiffness of the material. Therefore, low SNR might lead to inaccurate reconstruction of the stiffness estimates and possible appearance of artefacts.

McGarry *et al* [51] studied the influence of the OSS-SNR on the accuracy of elastographic reconstruction in single inclusion gelatine phantoms consisting of 5 % of weight for the background and 10 % for the inclusion. The results indicated accurate reconstruction of shear modulus of the background material at strain SNR above 3 with accurate reconstruction of stiffer inclusions for strain SNR above 5. The gelatine concentration used in this research for the tofu-gelatine phantom studies was also 10 %, which suggests thresholds for strain SNR of approximately 5.

Generally, relatively high SNR levels (above 5) were observed in both

phantoms across multiple frequencies, as depicted in Fig. 6. Assuming that OSS based SNR provides a reliable measure of the quality of MRE data, it is expected that SNR levels in phantoms studies do not influence inaccurate reconstruction results of the RD parameters. Therefore, the results presented here can be fully attributed to issues around model identifiability .

4.4. Other limitations

Additionally to noise, data-model mismatch can also contribute to significant degradation of the motion data quality, as any constitutive model provides only a continuum approximation of the great number of complex microscale interactions within the tissue matrix. Therefore, accuracy of the elastographic reconstruction results produced by such indirect SNLI algorithm can only be as good as the fundamental assumptions that underlie the constitutive model behaviour.

The reconstruction code models tissue as an isotropic nearly-incompressible linear RD elastic continuum. These assumptions allow identification of three parameters rather than the 21 that exist in a rank 4 strain tensor. However, the phantoms might display non-linear behaviour and be characterised by anisotropy and associated direction dependant properties. Hence, reconstruction results may not be accurate due to the fundamental data-model discrepancy caused by over-simplified model representation of the material mechanical properties. In this context, application of more sophisticated models, such as poroelasticity, might improve data-model fit. However, the increase in the number of unknown parameters being identified reinforces both high-resolution and high-SNR displacement images as well as complex model formulation.

Phase-wrapping is another challenging problem in MRE image acquisition. Depending on the pulse-sequence used, phase-errors can be introduced to the motion data which could lead to significant degradation of the image quality. These phase errors are mainly attributed to the excessive motion amplitudes of the induced actuation signal [8]. In this research, phase errors were corrected with the 3D quality-guided phase unwrapping technique introduced by Wang *et al* [45]. This correction leads to higher-quality MRE motion data and consequently higher-SNR level throughout imaging volume, and thus did not appear to affect the results.

5. Conclusion

This research presents a rigorous evaluation of the RD model in application to time-harmonic MRE. The full simultaneous three parameter-based reconstructions of RD based properties were performed on the damping phantoms, combining elastic and poroelastic medias. The main goal was to investigate the viability of the time-harmonic RD MRE in producing accurate recovery of VE properties as well as describing realistic damping behaviour.

Overall, good success was achieved in reconstruction of real shear modulus (μ_R) in both phantom configurations across multiple frequencies. Generally, μ_R images showed reasonable characterisation of both material types with acceptable delineation of the boundaries. However, reconstruction of RD properties, μ_I and ρ_I, yielded misleading effective property distributions resulting from model non-identifiability.

The non-identifiability of the RD model at a single frequency was demonstrated both from structural analysis and further confirmed by MRE phan-

tom experiments. In particular, RD reconstruction at a single frequency is highly structurally non-identifiable due to the similar model roles of the RD parameters. Such non-identifiability cannot be remediated by any number of regularisation techniques. Hence, the RD model is not recommended for medical imaging of delineating damping properties with a data obtained from a single frequency, which is a commonly used approach in a range of elastographic inverse problems used in biomedical applications of this model.

The structural analysis revealed that multiple frequencies are required for the RD model to accurately delineate the RD parameters, μ_I and ρ_I, and the resulting damping behaviour, expressed as a damping ratio ξ_d. An alternative approach of establishing practical identifiably of the RD model is the parametrisation, where one of the RD model parameters is globally constrained throughout the reconstructions domain, thus specifying its value. From medical imaging prospective, the simultaneous multifrequency inversion is the most promising approach for accurate reconstruction of the RD properties, which might provide additional diagnostic information.

Overall, use of an isotropic linear RD model to reconstruct data acquired in phantoms with MRE at a single frequency provided biased, highly variable results with regards to accurate mapping of damping properties. These findings suggest that the success with which RD model is applied to MRE data in tissue will depend on frequency range, number of frequencies at which the data is acquired, the underlying mechanical characteristics and the experimental compliance of the tissues and/or organs of clinical interest.

6. Acknowledgments

The authors would like to acknowledge Matthew McGarry from Dartmouth College of Engineering for help in data collection and Dr Elijah Van Houten from for providing valuable expertise in MRE.

References

[1] K. C. Siegmann, T. Xydeas, R. Sinkus, B. Kraemer, U. Vogel, and C. D. Claussen, "Diagnostic value of mr elastography in addition to contrast-enhanced mr imaging of the breastóinitial clinical results," *European radiology*, vol. 20, no. 2, pp. 318–325, 2010.

[2] A. Di Ieva, F. Grizzi, E. Rognone, Z. Tse, T. Parittotokkaporn, F. Rodriguez y Baena, M. Tschabitscher, C. Matula, S. Trattnig, and R. Rodriguez y Baena, "Magnetic resonance elastography: a general overview of its current and future applications in brain imaging," *Neurosurgical review*, vol. 33, no. 2, pp. 137–145, 2010.

[3] A. Sarvazyan, "Shear acoustic properties of soft biological tissues in medical diagnostics," *The Journal of the Acoustical Society of America*, vol. 93, p. 2329, 1993.

[4] M. Miga, K. Paulsen, F. Kennedy, P. Hoopes, A. Hartov, and D. Roberts, "Modeling surgical loads to account for subsurface tissue deformation during stereotactic neurosurgery," in *BiOS'98 International Biomedical Optics Symposium*. International Society for Optics and Photonics, 1998, pp. 501–511.

[5] C. J. Lewa and J. D. Certaines, "Mr imaging of viscoelastic properties," *Journal of Magnetic Resonance Imaging*, vol. 5, no. 2, pp. 242–244, 1995.

[6] R. Muthupillai, D. J. Lomas, P. J. Rossman, J. F. Greenleaf, A. Manduca, and R. L. Ehman, "Magnetic resonance elastography by direct visualization of propagating acoustic strain waves," *Science*, vol. 269, no. 5232, p. 1854, 1995.

[7] S. A. Kruse, M. A. Dresner, P. J. Rossman, J. P. Felmlee, C. R. Jack, and R. L. Ehman, ""palpation of the brain" using magnetic resonance elastography," in *ISMRM*. MR Research Laboratory, Mayo Clinic, 1999, p. 258.

[8] A. Manduca, T. E. Oliphant, M. A. Dresner, J. L. Mahowald, S. A. Kruse, E. Amromin, J. P. Felmlee, J. F. Greenleaf, and R. L. Ehman, "Magnetic resonance elastography: non-invasive mapping of tissue elasticity," *Medical Image Analysis*, vol. 5, no. 4, pp. 237–254, 2001.

[9] K. Uffmann, S. Maderwald, W. Ajaj, C. Galban, S. Mateiescu, H. Quick, and M. Ladd, "In vivo elasticity measurements of extremity skeletal muscle with mr elastography," *NMR in Biomedicine*, vol. 17, no. 4, pp. 181–190, 2004.

[10] J. Gennisson, C. Cornu, S. Catheline, M. Fink, and P. Portero, "Human muscle hardness assessment during incremental isometric contraction using transient elastography," *Journal of biomechanics*, vol. 38, no. 7, pp. 1543–1550, 2005.

[11] S. Papazoglou, J. Rump, J. Braun, and I. Sack, "Shear wave group velocity inversion in mr elastography of human skeletal muscle," *Magnetic resonance in medicine*, vol. 56, no. 3, pp. 489–497, 2006.

[12] S. Bensamoun, S. Ringleb, L. Littrell, Q. Chen, M. Brennan, R. Ehman, and K. An, "Determination of thigh muscle stiffness using magnetic resonance elastography," *Journal of Magnetic Resonance Imaging*, vol. 23, no. 2, pp. 242–247, 2005.

[13] E. Van Houten, M. Doyley, F. Kennedy, J. Weaver, and K. Paulsen, "Initial in vivo experience with steady-state subzone-based mr elastography of the human breast," *Journal of Magnetic Resonance Imaging*, vol. 17, no. 1, pp. 72–85, 2002.

[14] D. Plewes, J. Bishop, A. Samani, and J. Sciarretta, "Visualization and quantification of breast cancer biomechanical properties with magnetic resonance elastography," *Physics in Medicine and Biology*, vol. 45, no. 6, p. 1591, 2000.

[15] R. Sinkus, M. Tanter, S. Catheline, J. Lorenzen, C. Kuhl, E. Sondermann, and M. Fink, "Imaging anisotropic and viscous properties of breast tissue by magnetic resonance-elastography," *Magnetic resonance in medicine*, vol. 53, no. 2, pp. 372–387, 2005.

[16] A. McKnight, J. Kugel, P. Rossman, A. Manduca, L. Hartmann, and R. Ehman, "Mr elastography of breast cancer: preliminary results," *American Journal of Roentgenology*, vol. 178, no. 6, pp. 1411–1417, 2002.

[17] J. Lorenzen, R. Sinkus, M. Lorenzen, M. Dargatz, C. Leussler, P. Röschmann, G. Adam *et al.*, "Mr elastography of the breast: preliminary clinical results." *RoFo: Fortschritte auf dem Gebiete der Rontgenstrahlen und der Nuklearmedizin*, vol. 174, no. 7, p. 830, 2002.

[18] O. Rouvière, M. Yin, M. Dresner, P. Rossman, L. Burgart, J. Fidler, and R. Ehman, "Mr elastography of the liver: Preliminary results1," *Radiology*, vol. 240, no. 2, pp. 440–448, 2006.

[19] S. Venkatesh, M. Yin, J. Glockner, N. Takahashi, P. Araoz, J. Talwalkar, and R. Ehman, "Mr elastography of liver tumors: preliminary results," *American Journal of Roentgenology*, vol. 190, no. 6, pp. 1534–1540, 2008.

[20] P. Asbach, D. Klatt, U. Hamhaber, J. Braun, R. Somasundaram, B. Hamm, and I. Sack, "Assessment of liver viscoelasticity using multifrequency mr elastography," *Magnetic Resonance in Medicine*, vol. 60, no. 2, pp. 373–379, 2008.

[21] S. Kruse, R. Grimm, D. Lake, A. Manduca, and R. Ehman, "Fast EPI Based 3D MR Elastography of the Brain," in *Proc. Intl. Soc. Mag. Reson. Med*, vol. 14, 2006, p. 3385.

[22] M. Green, R. Sinkus, and L. E. Bilston, "High resolution 3d brain mr-elastography," in *ISMRM*, 2006, p. 2021.

[23] S. A. Kruse, G. H. Rose, K. J. Glaser, A. Manduca, J. P. Felmlee, C. R. Jack, and R. L. Ehman, "Magnetic resonance elastography of the brain," *Neuroimage*, vol. 39, no. 1, pp. 231–237, 2007.

[24] L. Xu, Y. Lin, Z. N. Xi, H. Shen, and P. Y. Gao, "Magnetic resonance elastography of the human brain: a preliminary study," *Acta Radiologica*, vol. 48, no. 1, pp. 112–115, 2007.

[25] D. Klatt, U. Hamhaber, P. Asbach, J. Braun, and I. Sack, "Noninvasive assessment of the rheological behavior of human organs using multifrequency mr elastography: a study of brain and liver viscoelasticity," *Physics in Medicine and Biology*, vol. 52, no. 24, pp. 7281–7294, 2007.

[26] I. Sack, B. Beierbach, U. Hamhaber, D. Klatt, and J. Braun, "Noninvasive measurement of brain viscoelasticity using magnetic resonance elastography," *NMR in Biomedicine*, vol. 21, no. 3, pp. 265–271, 2007.

[27] M. A. Green, L. E. Bilston, and R. Sinkus, "In vivo brain viscoelastic properties measured by magnetic resonance elastography," *NMR in Biomedicine*, vol. 21, no. 7, pp. 755–764, 2008.

[28] I. Sack, B. Beierbach, J. Wuerfel, D. Klatt, U. Hamhaber, S. Papazoglou, P. Martus, and J. Braun, "The impact of aging and gender on brain viscoelasticity," *Neuroimage*, vol. 46, no. 3, pp. 652–657, 2009.

[29] J. Wuerfel, F. Paul, B. Beierbach, U. Hamhaber, D. Klatt, S. Papazoglou, F. Zipp, P. Martus, J. Braun, and I. Sack, "Mr-elastography reveals degradation of tissue integrity in multiple sclerosis," *Neuroimage*, vol. 49, no. 3, pp. 2520–5, Feb 2010.

[30] I. Perreard, A. Pattison, M. Doyley, M. McGarry, Z. Barani, E. Van Houten, J. Weaver, and K. Paulsen, "Effects of frequency-and

direction-dependent elastic materials on linearly elastic mre image reconstructions," *Physics in medicine and biology*, vol. 55, no. 22, p. 6801, 2010.

[31] P. Perriez, F. Kennedy, E. Van Houten, J. Weaver, and K. Paulsen, "Magnetic resonance poroelastography: an algorithm for estimating the mechanical properties of fluid-saturated soft tissues," *Medical Imaging, IEEE Transactions on*, vol. 29, no. 3, pp. 746–755, 2010.

[32] M. McGarry, H. Berger, and E. Van Houten, "Damping models in elastography," in *Medical Imaging*. International Society for Optics and Photonics, 2007, pp. 65 111W–65 111W.

[33] W. G. Bradley Jr, A. R. Whittemore, A. S. Watanabe, S. J. Davis, L. M. Teresi, and M. Homyak, "Association of deep white matter infarction with chronic communicating hydrocephalus: implications regarding the possible origin of normal-pressure hydrocephalus," *American Journal of Neuroradiology*, vol. 12, no. 1, p. 31, 1991.

[34] M. McGarry and E. Van Houten, "Use of a rayleigh damping model in elastography," *Medical and Biological Engineering and Computing*, vol. 46, no. 8, pp. 759–766, 2008.

[35] E. Van Houten, M. Doyley, F. Kennedy, K. Paulsen, and J. Weaver, "A three-parameter mechanical property reconstruction method for mr-based elastic property imaging," *Medical Imaging, IEEE Transactions on*, vol. 24, no. 3, pp. 311–324, 2005.

[36] S. Audoly, G. Bellu, L. D'Angio, M. Saccomani, and C. Cobelli, "Global identifiability of nonlinear models of biological systems," *Biomedical Engineering, IEEE Transactions on*, vol. 48, no. 1, pp. 55–65, 2001.

[37] M. Pia Saccomani, S. Audoly, and L. D'Angiò, "Parameter identifiability of nonlinear systems: the role of initial conditions," *Automatica*, vol. 39, no. 4, pp. 619–632, 2003.

[38] G. Bellu, M. Saccomani, S. Audoly, and L. DíAngiò, "Daisy: A new software tool to test global identifiability of biological and physiological systems," *Computer methods and programs in biomedicine*, vol. 88, no. 1, p. 52, 2007.

[39] E. E. W. Van Houten, M. I. Miga, J. B. Weaver, F. E. Kennedy, and K. D. Paulsen, "Three-dimensional subzone-based reconstruction algorithm for mr elastography," *Magnetic Resonance in Medicine*, vol. 45, no. 5, pp. 827–837, 2001.

[40] A. A. Oberai, N. H. Gokhale, and G. R. Feijóo, "Solution of inverse problems in elasticity imaging using the adjoint method," *Inverse Problems*, vol. 19, no. 2, p. 297, 2003.

[41] A. Chambolle, "An algorithm for total variation minimization and applications," *Journal of Mathematical imaging and vision*, vol. 20, no. 1, pp. 89–97, 2004.

[42] J. Ritt, *Differential algebra*. Amer Mathematical Society, 1950, vol. 33.

[43] J. Wu, "Tofu as a tissue-mimicking material," *Ultrasound in medicine & biology*, vol. 27, no. 9, pp. 1297–1300, 2001.

[44] R. Righetti, J. Ophir, S. Srinivasan, T. Krouskop *et al.*, "The feasibility of using elastography for imaging the poisson's ratio in porous media," *Ultrasound in medicine & biology*, vol. 30, no. 2, pp. 215–228, 2004.

[45] H. Wang, J. Weaver, I. Perreard, M. Doyley, and K. Paulsen, "A three-dimensional quality-guided phase unwrapping method for mr elastography," *Physics in Medicine and Biology*, vol. 56, p. 3935, 2011.

[46] E. Van Houten, K. Paulsen, M. Miga, F. Kennedy, J. Weaver *et al.*, "An overlapping subzone technique for mr-based elastic property reconstruction," *Magnetic resonance in medicine*, vol. 42, no. 4, pp. 779–786, 1999.

[47] M. McGarry, E. Van Houten, C. Johnson, J. Georgiadis, B. Sutton, J. Weaver, and K. Paulsen, "Multiresolution mr elastography using nonlinear inversion," *Medical Physics*, vol. 39, p. 6388, 2012.

[48] G. H. Golub, P. C. Hansen, and D. P. O'Leary, "Tikhonov regularization and total least squares," *SIAM Journal on Matrix Analysis and Applications*, vol. 21, no. 1, pp. 185–194, 1999.

[49] P. Docherty, J. Chase, T. Lotz, T. Desaive *et al.*, "A graphical method for practical and informative identifiability analyses of physiological models: A case study of insulin kinetics and sensitivity," *Biomedical engineering online*, vol. 10, no. 1, pp. 1–20, 2011.

[50] E. Van Houten, M. McGarry, P. Perrinez, I. Perreard, J. Weaver, and K. Paulsen, "Subzone based magnetic resonance elastography using a

rayleigh damped material model," *Medical Physics*, vol. 38, p. 1993, 2011.

[51] M. McGarry, E. Van Houten, P. Perrinez, A. Pattison, J. Weaver, and K. Paulsen, "An octahedral shear strain-based measure of snr for 3d mr elastography," *Physics in Medicine and Biology*, vol. 56, p. N153, 2011.